

# FIELD IMAGING RADAR/LIDAR THROUGH FOURIER TRANSFORM HETERODYNE

January 1999

Bradly J. Cooke, Amy E. Galbraith<sup>†</sup>, Bryan E. Laubscher, Charlie E. Strauss,  
Nicholas L. Olivas, and Andrew C. Grubler<sup>‡</sup>

Los Alamos National Laboratory  
P.O. Box 1663, MS-D448  
Los Alamos, NM 87545

## ABSTRACT

We present a detection process capable of directly imaging the transverse amplitude, phase, and Doppler shift of coherent electromagnetic fields. Based on coherent detection principles governing conventional heterodyned RADAR/LIDAR systems, Fourier Transform Heterodyne incorporates transverse spatial encoding of the reference local oscillator for image capture. Appropriate selection of spatial encoding functions allows image retrieval by way of classic Fourier manipulations. Of practical interest: (i) imaging may be accomplished with a single element detector/sensor requiring no additional scanning or moving components, (ii) as detection is governed by heterodyne principles, near quantum limited performance is achievable, (iii) a wide variety of appropriate spatial encoding functions exist that may be adaptively configured in real-time for applications requiring optimal detection, and (iv) the concept is general with the applicable electromagnetic spectrum encompassing the RF through optical.

## 1.0 INTRODUCTION

The ability to spatially image and manipulate both amplitude and phase of RF through optical coherent electromagnetic fields enables interesting adaptations of current RADAR and LIDAR systems. Candidate RADAR/LIDAR functions potentially enhanced through exploitation of spatial field imaging include target classification and identification, Doppler field imaging, adaptive spatial filtering optimizing target discrimination and/or suppression of electronic counter measures, and coherently phased sparse arrays for improved spatial resolution and detection of low cross-section targets. As will be demonstrated in this paper, intrinsic to heterodyne square-law detection physics is the ability to detect and manipulate spatial field states as well as the temporal state through a process named Fourier Transform Heterodyne (FTH). As a result, FTH based field imaging introduces the spatial dimension via a detection process fully analogous and complimentary with existing RADAR and LIDAR concepts and technology.

---

<sup>†</sup> Electrical and Computer Engineering Department, University of Arizona

<sup>‡</sup> United States Naval Academy, P.O. Box 12939, Annapolis, MD 21412

## Form SF298 Citation Data

|   |  |   |
|---|--|---|
| <b>Report Date</b><br><i>("DD MON YYYY")</i><br>00011999  | <b>Report Type</b><br>N/A                      | <b>Dates Covered (from... to)</b><br><i>("DD MON YYYY")</i> |
| <b>Title and Subtitle</b><br>Field Imaging Radar/Lidar Through Fourier Transform<br>Heterodyne  |  | <b>Contract or Grant Number</b>                             |
| <b>Authors</b>  |  | <b>Program Element Number</b>                               |
| <b>Performing Organization Name(s) and Address(es)</b><br>Los Alamos National Laboratory P.O. Box 1663, MS-D448 Los<br>Alamos, NM 87545 |  | <b>Project Number</b>                                       |
| <b>Sponsoring/Monitoring Agency Name(s) and Address(es)</b>   |  | <b>Task Number</b>  |
| <b>Distribution/Availability Statement</b><br>Approved for public release, distribution unlimited                                       |  | <b>Work Unit Number</b>                                     |
| <b>Supplementary Notes</b>  |  | <b>Performing Organization Number(s)</b>                    |
| <b>Abstract</b>   |  | <b>Monitoring Agency Acronym</b>                            |
| <b>Subject Terms</b>  |  | <b>Monitoring Agency Report Number(s)</b>                   |
| <b>Document Classification</b><br>unclassified  | <b>Classification of SF298</b><br>unclassified |   |
| <b>Classification of Abstract</b><br>unclassified   | <b>Limitation of Abstract</b><br>unlimited     |   |
| <b>Number of Pages</b><br>20  |  |   |

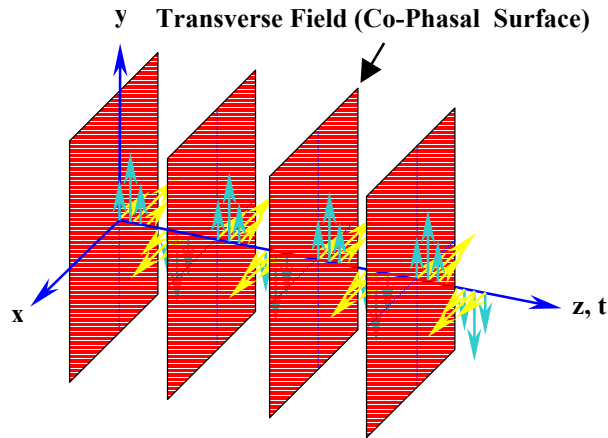


**Figure 1.** Transverse and longitudinal components of propagating electromagnetic field.

photosensitive device subjects the transverse field to a process referred to as squared modulus or square-law detection.<sup>2</sup> The square-law imaging of a complex field composed of a spatial amplitude and phase distribution,  $\Phi_{Image}$ , results in the observer imaging the field's *intensity*<sup>3</sup>

$$\mathbf{I}_i \propto |\Phi_{Image}|^2, \quad [1]$$

with all phase information lost. Preservation of *both* spatial amplitude and phase prompts a detection process that sidesteps the limitations imposed by the square-law operation.

The goal of this paper is the introduction of a heterodyned imaging detection process that circumvents the square-law limitations, and therefore, is capable of directly imaging the transverse amplitude and phase of coherent electromagnetic fields. **Section 2** introduces the underlying principles governing FTH field detection through the calculus of Fourier spatial projection operators, while **Section 3** demonstrates Fourier projection concepts and field imaging via a simple experimental setup based on a HeNe laser and a 69 element spatial phase modulator. Finally, practical considerations and potential RADAR/LIDAR applications exploiting spatial field imaging are discussed in **Section 4**. It should be noted that while the emphasis of this paper is on systems operating in sub-millimeter through optical wavelengths (i.e. physical-optics approximation<sup>4</sup> where the transverse dimensions of the field, aperture, and other surface curvatures are large compared to wavelength), the theory is relatively general and in many cases is readily extended to longer wavelength systems.

## 2.0 FOURIER TRANSFORM HETERODYNE

### 2.1 Fourier Projection Operator

Central to FTH field imaging are Fourier projection concepts based on square-law heterodyne detection principles relating the spatial distribution of an image field,  $\Phi_{Image}$ , to that of a (typically user defined) reference field,  $\Phi_{Ref}$ .

### 1.1 Field Imaging

The transverse and longitudinal components of a propagating coherent electromagnetic field are shown in **Figure 1**. The spatial amplitude and phase distributions comprising the transverse field lie in a two-dimensional surface normal to the longitudinal direction of propagation with constant phase surfaces spaced a wavelength apart<sup>1</sup>. The propagating field conveys spatial information to an observer at  $\mathbf{z}$  through the temporal variations in the spatial amplitude and phase distribution. Observing (imaging) the field with eyes, film, CCD camera or other

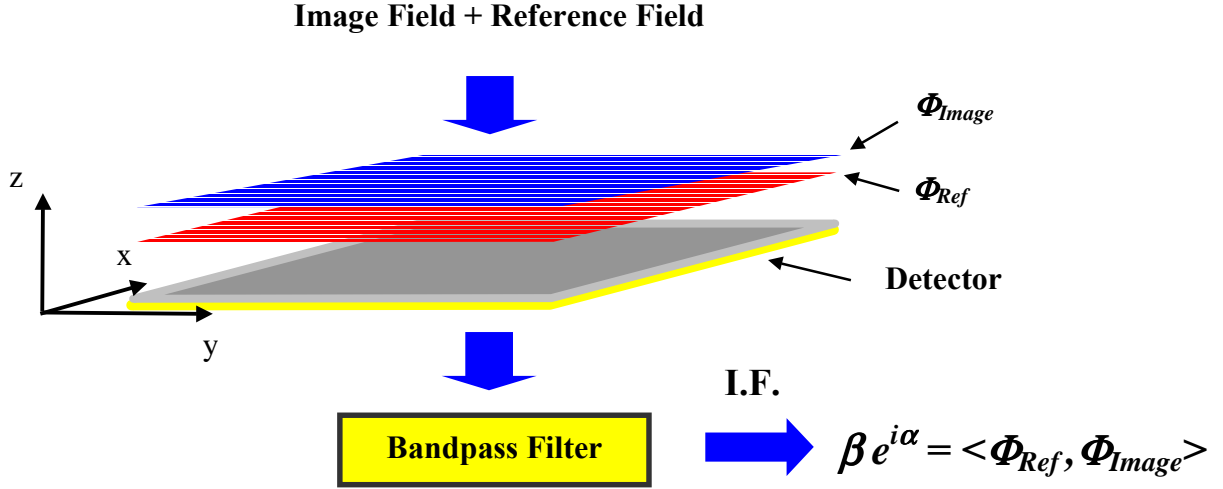


**Figure 2.** Heterodyned square-law detection can be perceived as a Fourier projection with the intermediate frequency (I.F.) current conveying the magnitude ( $\beta$ ) and phase ( $\alpha$ ) of the projection.

Referring to **Figure 2**, the heterodyning of the image field,  $\Phi_{Image}$ , with the reference field,  $\Phi_{Ref}$ , in a square-law detector of surface area,  $s$ , results (after filtering) in a complex intermediate frequency (I.F.) current. As will be demonstrated, the magnitude ( $\beta$ ) and phase ( $\alpha$ ) of the I.F. current conveys the spatial Fourier projection of the reference field onto the image field

$$\beta e^{i\alpha} = \langle \Phi_{Ref}, \Phi_{Image} \rangle \equiv \iint_s \Phi_{Image} \Phi_{Ref}^* dx dy. \quad [2]$$

The derivation of **Equation 2** follows from Poynting's relation<sup>5,6,7</sup> which relates the induced detector current,  $I$ , to the detector's quantum efficiency,  $\eta$ , and the spatial distribution of the image and reference electromagnetic fields,  $\Phi_{Image}$  and  $\Phi_{Ref}$  respectively, over the detector surface,  $s$ , through

$$I = k \iint_s \eta (\mathbf{E} \times \mathbf{H}) \cdot d\mathbf{s} \quad [\text{Ampere}], \quad [3]$$

where

$$\mathbf{E} = \Phi_{Image} + \Phi_{Ref}, \quad \mathbf{H} = \mathbf{H}_{Image} + \mathbf{H}_{Ref}, \quad k = \text{constant}. \quad [4]$$

Assuming the image and reference fields are transverse electromagnetic in nature,

$$\Phi_{Image} = \rho(x, y) e^{-i\omega t - i\phi(x, y)}, \quad [5]$$

$$\Phi_{Ref} = A e^{-i\omega' t - i\theta(x, y)}, \quad [6]$$

and the reference fields form a complete orthonormal<sup>8</sup> basis set such that

$$\iint_s e^{i\theta(k_x, k_y, x, y)} e^{-i\theta(k'_x, k'_y, x, y)} dx dy = \delta(k_x - k'_x) \delta(k_y - k'_y), \quad [7]$$

then the detector current at the intermediate frequency,  $\Delta\omega = \omega - \omega'$ , reduces to

$$I(k_x, k_y, \Delta\omega) = 2k A \eta \sqrt{\frac{\mathcal{E}}{\mu}} \operatorname{Re} \left[ \iint_s \Phi_{Image}(x, y) e^{i\omega' t + i\theta(k_x, k_y, x, y)} dx dy \right] \quad [8]$$

$$= 2k A \sqrt{\frac{\mathcal{E}}{\mu}} \beta(k_x, k_y) \cos(\Delta\omega t + \alpha(k_x, k_y)) \quad [\text{Ampere}]. \quad [9]$$

Complex Fourier coefficients,  $C(k_x, k_y) \propto \beta(k_x, k_y) e^{i\alpha(k_x, k_y)}$ , can then be formed from the I.F. current's complex phase and magnitude, resulting in the following transform pair relating the image field, complex Fourier coefficient and reference basis set:

$$C(k_x, k_y) = \iint_s \Phi_{Image}(x, y) e^{i\theta(k_x, k_y, x, y)} dx dy \Leftrightarrow \Phi_{Image}(x, y) = \iint_s C(k_x, k_y) e^{-i\theta(k_x, k_y, x, y)} dk_x dk_y. \quad [10]$$

In general, spatial variations may be present in both the reference beam and detection quantum efficiency. Taking these variations into account, **Equation 8** would be rewritten as

$$I(k_x, k_y, \Delta\omega) = 2k \sqrt{\frac{\mathcal{E}}{\mu}} \operatorname{Re} \left[ \iint_s \eta(x, y) \Phi_{Image}(x, y) \Phi_{Ref}(x, y)^* dx dy \right], \quad [11]$$

$$\text{with } \Phi_{Ref}(x, y) = \rho'(x, y) e^{-i\omega' t - i\theta(x, y)}. \quad [12]$$

Finally, if the image field is heterodyned with a discrete set of reference fields ( $\Phi_{Ref}(x, y) \rightarrow \Phi_{m,n}$ ), then **Equation 11** reduces to the following Fourier expansion pair

$$\Phi_{Image}(x, y, \Delta\omega_l) = \Phi_{Image}(x, y, l) = \sum_m \sum_n C_{l,m,n} \Phi_{m,n}(x, y), \quad [13]$$

$$C_{l,m,n} = \langle \Phi_{m,n}, \Phi_{Image} \rangle, \quad \langle \Phi_{m,n}, \Phi_{Image} \rangle \equiv \iint_s \Phi_{Image} \Phi_{m,n}^* dx dy. \quad [14]$$

The bracket operator notation of **Equation 2** has been introduced to simplify notation. Additionally, the index  $l$ , representing the  $l^{th}$  I.F. bandpass frequency ( $\Delta\omega$ ) has been included to account for Doppler shifts.

Of practical interest in the development of synthetic apertures and multi-element detectors (such as focal plane arrays and phased array<sup>9</sup> receivers), the detecting surface,  $s$ , can be partitioned into multiple detection surfaces and coherently summed in the following manner

$$\iint_s \Phi_{Image} \Phi_{m,n}^* dx dy \Rightarrow \sum_{s_i} \iint_{s_i} \Phi_{Image} \Phi_{m,n}^* dx dy. \quad [15]$$

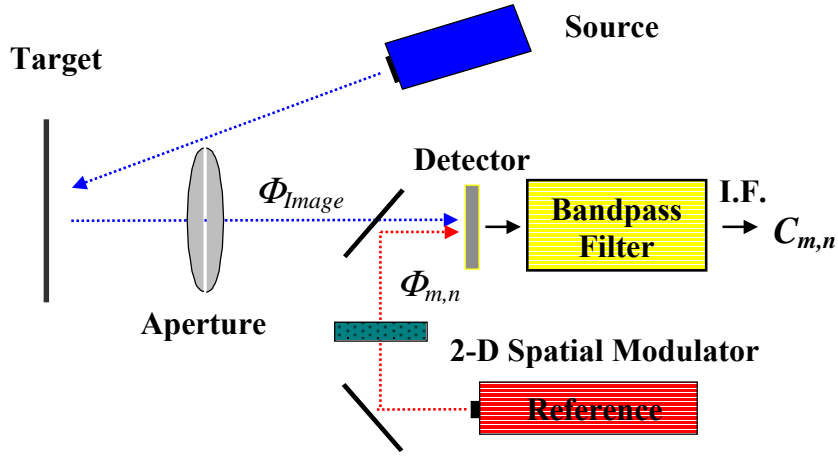


**Figure 3.** Fourier transform heterodyne field imaging. Based on coherent detection principles, FTH applies Fourier projection concepts through the transverse spatial encoding ( $\Phi_{m,n}$ ) of the local oscillator for electromagnetic field capture. FTH preserves both spatial amplitude and phase information.

Finally, generalized to three-dimensional (3-D) surfaces, the Fourier projection operator conveys the degree of correlation between image and reference fields,

$$\iint_s \mathbf{J} \cdot d\mathbf{s} = k \iint_s \eta(\mathbf{E} \times \mathbf{H}) \cdot d\mathbf{s} \Leftrightarrow \langle \Phi_{Ref}(x, y, z, t, \mathbf{p}, \lambda), \Phi_{Image}(x, y, z, t, \mathbf{p}, \lambda) \rangle, \quad [16]$$

where  $\mathbf{J}$  is the induced current density,  $t$  the time variable,  $\mathbf{p}$  the field polarization and  $\lambda$  the wavelength. The projection is maximized when image and reference field states are matched (matched filter condition). Field states may be tailored to introduce signal uniqueness, and/or noise & clutter suppression for the design of optimal detection processes. Spatial and temporal field states include time, frequency, polarization, and spatial amplitude & phase.

## 2.2 FTH Field Imaging

Applying **Equations 13 - 14**, and referring to **Figure 3**, the basic steps involved in image field capture follow:

- Heterodyne the image field,  $\Phi_{Image}$ , with the local oscillator (l.o.) whose transverse amplitude and phase is sequentially modulated with a known set of reference spatial phase functions,  $\Phi_{Ref} = \Phi_{m,n}$ , that span a valid basis set.
- Measure the projected detector current's magnitude and phase and form the complex Fourier coefficient,  $C_{m,n}$ , for each spatial function,  $\Phi_{m,n}$ .
- Through **Equation 13**, reconstruct the image field from the basis functions,  $\Phi_{m,n}$ , and the measured  $C_{m,n}$ :

$$\Phi_{Image}(x, y) = \sum_m \sum_n C_{m,n} \Phi_{m,n}(x, y).$$

While a single element system is demonstrated in **Figure 3**, image capture rates may be improved through reference field partitioning and multi-element detection (see **Equation 15**).

### 3.0 EXPERIMENT

A simple experiment demonstrating the FTH concept has been constructed. Illustrated in **Figure 4** with photographed apparatus in **Figure 5**, the experiment implements a Zeeman split HeNe laser ( $\Delta f = 250$  kHz) for source and local-oscillator lines, and a 69 element spatial phase modulator to encode the 36 term basis used in the experiment. A description of the experimental procedure follows:

- The two orthogonally polarized laser lines ( $\Delta f = 250$  kHz) at the output of the HeNe laser are separated with the polarizing beam splitter into two beams paths.
- The first beam illuminates the target forming the image,  $\Phi_{Image}$ , while the second beam passes through the 69-element spatial modulator generating the  $n^{th}$  reference term,  $\Phi_n$ ,  $n = 0, 1, \dots, 35$ .
- The two beams are recombined and heterodyned at the single-element silicon detector generating a 250 kHz intermediate frequency current  $I_n$ .
- A digital oscilloscope measures the 250 kHz I.F. current's phase and magnitude from which the Fourier coefficients,  $C_n$ , are formed (see **Figure 6**).
- Once all 36 basis coefficients,  $C_n$ ,  $n = 0, 1, \dots, 35$ , are sequentially measured, the resulting magnitude and phase of the detected image,  $\Phi_{Image}$ , are displayed on the computer screen.

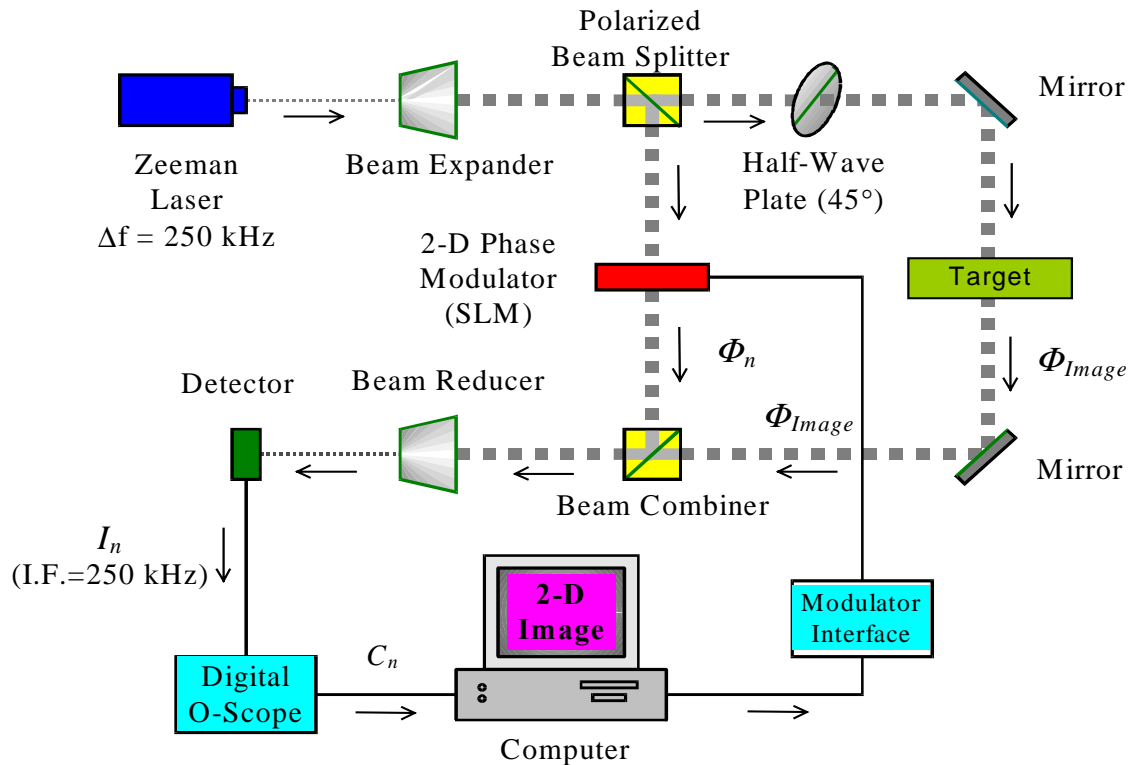


**Figure 4.** Schematic diagram of FTH experiment.

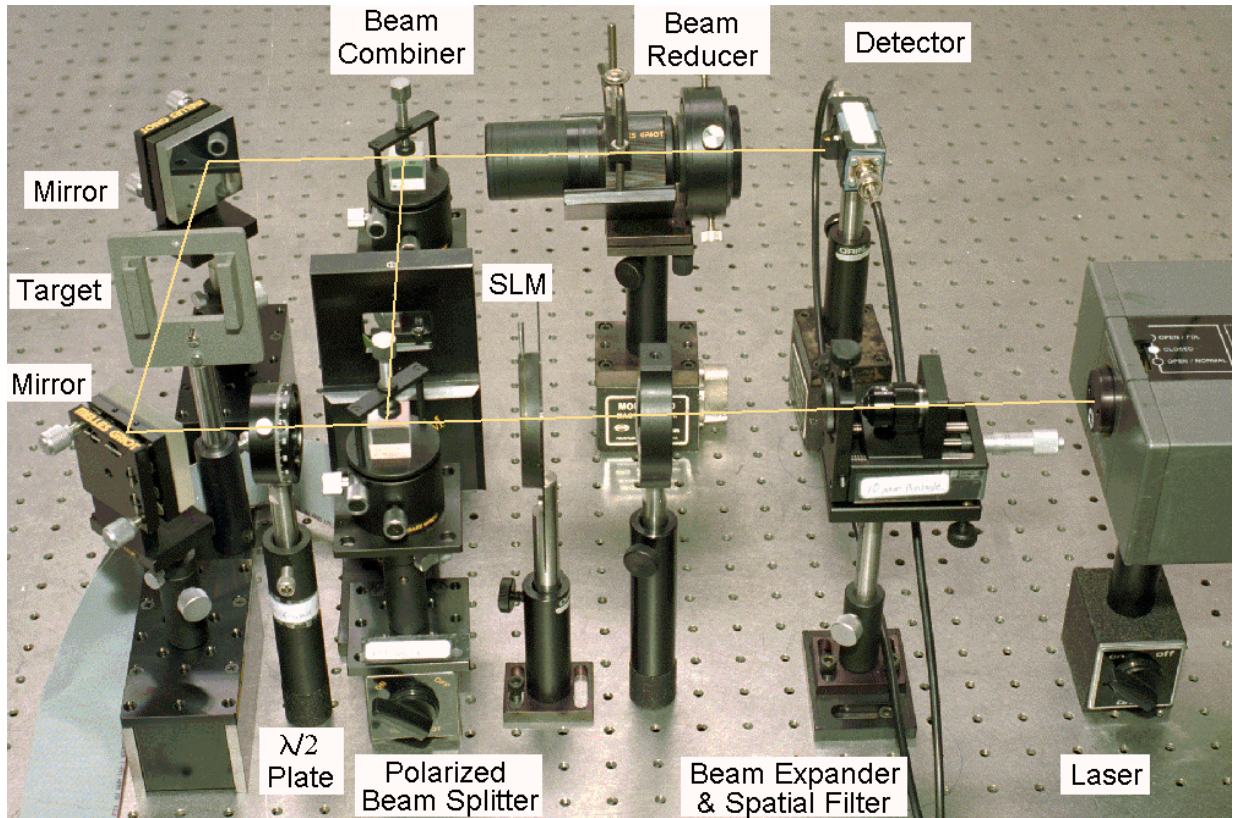


Figure 5. Experimental apparatus.

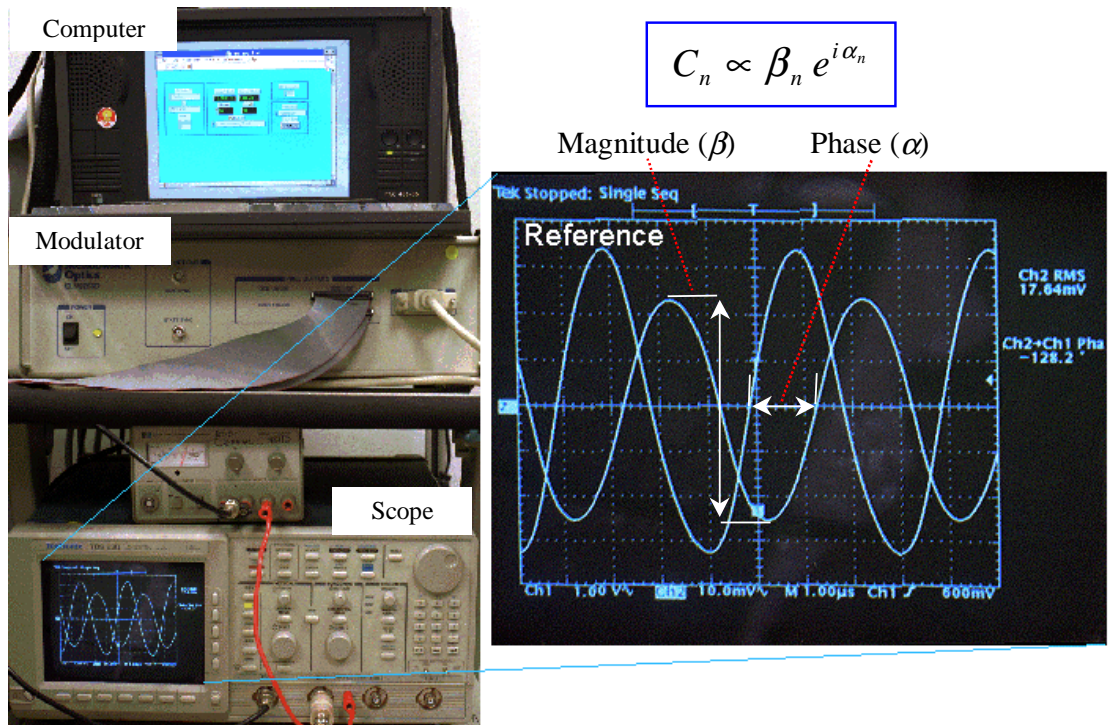
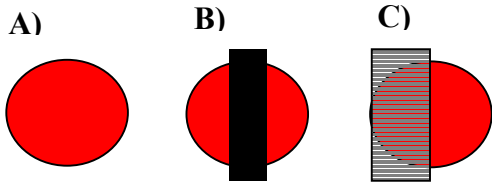


Figure 6. A digital oscilloscope measures the 250 kHz I.F. current's phase and magnitude from which the Fourier coefficients,  $C_n$ , are formed.

The 2-D spatial phase modulator, implemented to encode the reference beam phase front, is the commercially produced Meadowlark Optics Hex69 spatial light modulator (SLM). The Meadowlark SLM is a 69 pixel, two-dimensional array of hexagon shaped, liquid-crystal variable retarders developed for real time programmable phase masking applications. As Meadowlark Optics conveniently supplies the software to generate the first 36 terms of the Zernike<sup>10</sup> polynomial expansion set, the Zernike set was adopted for the experiment and **Equation 12**, in circular coordinates, takes on the form

$$\Phi_{ref} \rightarrow \Phi_n = \rho'(r, \theta) e^{-i\omega t - i 2\pi Z_n(r, \theta)}, \quad n = 0, 1, \dots, 35. \quad [17]$$



The beam targets employed in the experiment are catalogued in **Figure 7**. Note that commensurate with the rather limited 36-term expansion set, simple target geometry was maintained throughout the experiment.

**Figure 7.** Beam targets: A) No target, B) 1/3 Center block, C) 1/2 Dielectric block (glass microscope slide with transmission  $T = 90\%$  and phase shift  $\Delta\theta = 0.9\pi$ ).

For the purpose of providing a comparative baseline between measurement and theory, the complex coefficients were directly evaluated from **Equation 14** resulting in

$$C_n = \int_0^{2\pi} \int_0^1 T(r, \theta) \rho(r, \theta) \rho'(r, \theta) e^{2\pi i Z_n(r, \theta)} r dr d\theta, \quad n = 0, 1, \dots, 35, \quad [18]$$

with

$T(r, \theta) \equiv$  beam targets of **Figure 7**,

$\rho(r, \theta) = \rho'(r, \theta) = 1$  for a plane wave, and

$\rho(r, \theta) = \rho'(r, \theta) = e^{-\frac{r^2}{\omega^2}}$  for a simple Gaussian beam<sup>11</sup>.

From **Equation 13**, given the measured coefficients, the field image is expanded through

$$\Phi_{Image}(r, \theta) = \sum_n C_n \Phi_n(r, \theta), \quad n = 0, 1, \dots, 35, \quad [19]$$

and the intensity (energy) evaluated with

$$Intensity(r, \theta) = \left| \Phi_{Image}(r, \theta) \right|^2. \quad [20]$$

Plotted in **Figure 8** are measured spectral coefficients (no target) along with the calculated spectral coefficients for the simple plane wave and Gaussian ( $\omega = 1/2$ ) models.

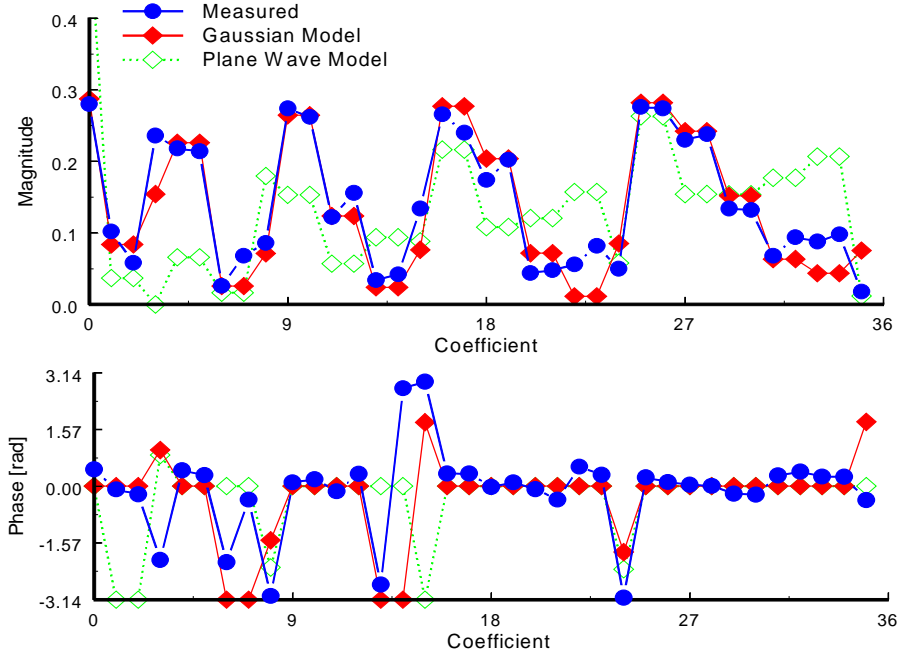


**Figure 8.** Measured spectral coefficients for no target. Included are plane-wave and Gaussian ( $\omega = 1/2$ ) coefficients for baseline comparison (coefficients have been normalized) with Gaussian model providing the best fit.

The Gaussian model was evaluated for the remaining targets of **Figure 7**, generating baseline comparison with measurements. The theoretically predicted and experimentally measured amplitude, phase, and intensity (energy) for the beam targets of **Figure 7** are plotted in **Figures 9 – 11**. Both calculated and measured coefficients are normalized and a constant phase offset was added to the measured coefficients, equalizing pedestal/piston. **Figure 11** was further subjected to the linear transform, described next, to clarify the phase image.

A consequence of raising the Zernike polynomials to an exponent, as prescribed by **Equation 12**, is noted in the fact that the 36-term basis set is no longer orthogonal. A non-orthogonal basis set will result in the off diagonal coupling of the expansion coefficients which, depending on coupling strength and image spectrum, can in turn degrade image fidelity. The magnitude of off diagonal coupling of **Equation 17** is on the order of a rather high 5% - 10%. The coefficients can be decoupled through the following linear transform<sup>12</sup>

$$\mathbf{C} \rightarrow \mathbf{\Lambda}^{-1} \mathbf{C}, \quad [21]$$

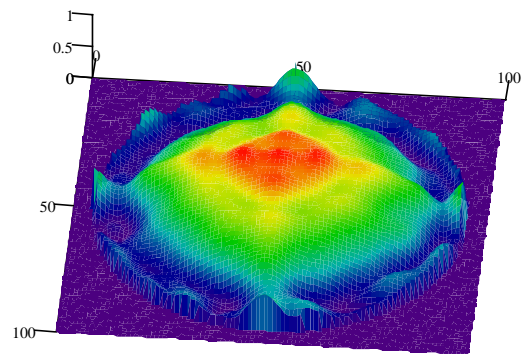
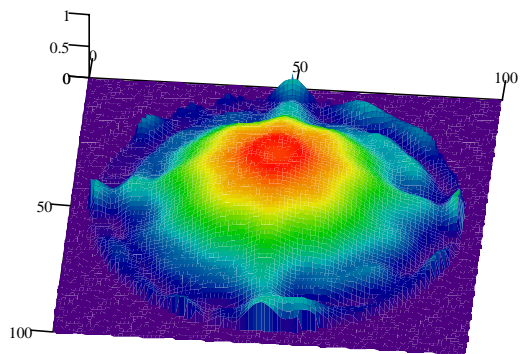
where:

$$\mathbf{\Lambda} = \begin{bmatrix} \langle Z_0, Z_0 \rangle & \cdots & \langle Z_0, Z_{35} \rangle \\ \vdots & \ddots & \vdots \\ \langle Z_{35}, Z_0 \rangle & \cdots & \langle Z_{35}, Z_{35} \rangle \end{bmatrix},$$

$$\text{and } \langle Z_p, Z_q \rangle = \int_0^1 \int_0^{2\pi} e^{-2\pi i Z_p(r, \theta)} e^{2\pi i Z_q(r, \theta)} r dr d\theta. \quad [22]$$

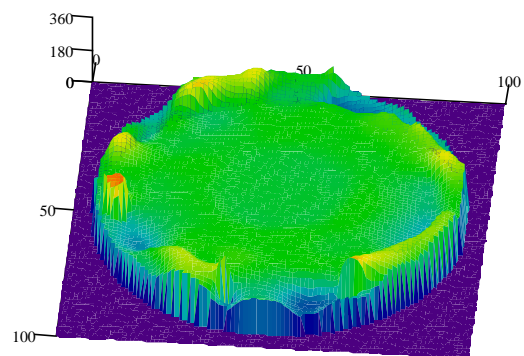
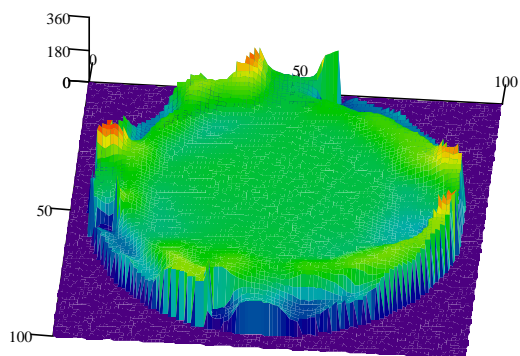
**A) Gaussian Model**

**B) Measured**



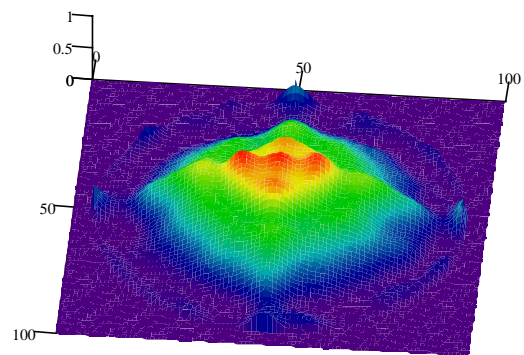
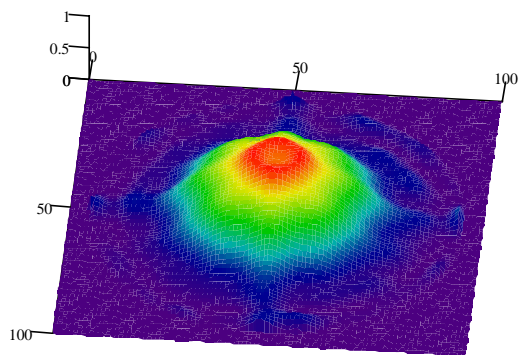
Amplitude

Amplitude



Phase

Phase



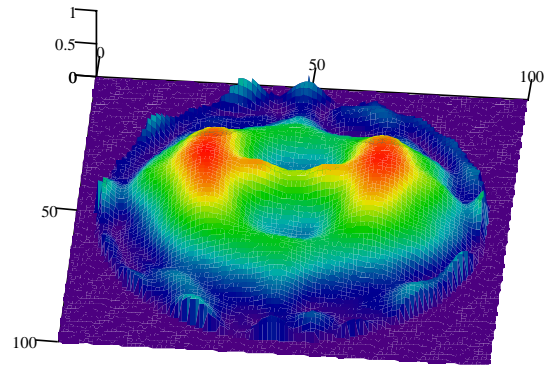
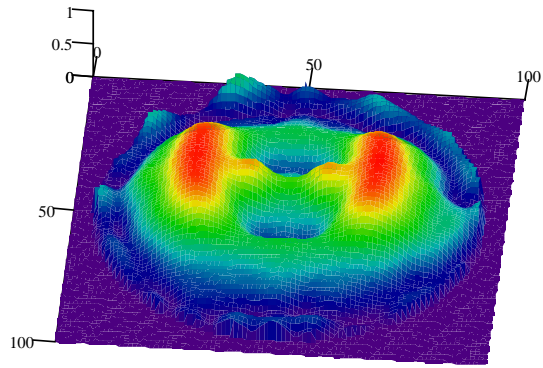
Intensity

Intensity

**Figure 9.** No target. **A)** Theoretically predicted and **B)** Experimentally measured amplitude, phase, and intensity.

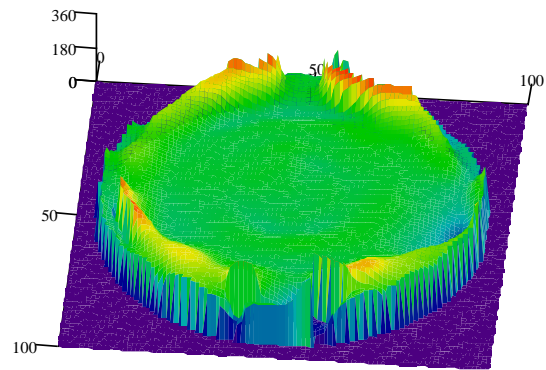
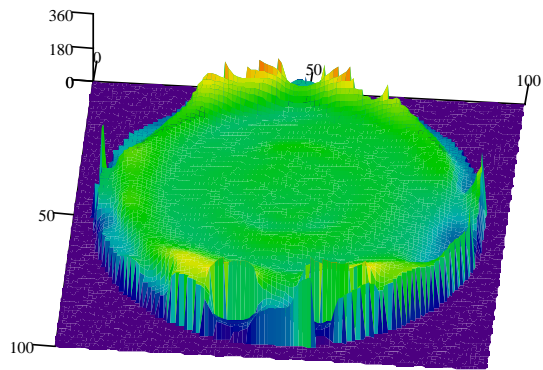
**A) Gaussian Model**

**B) Measured**



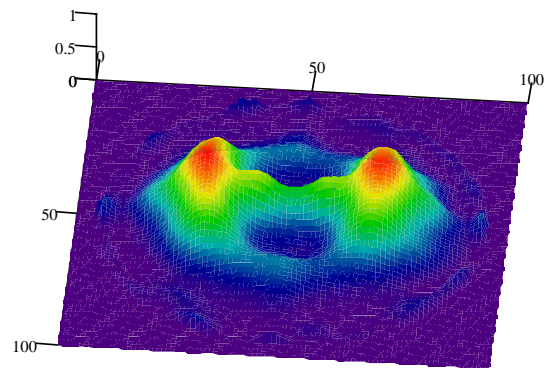
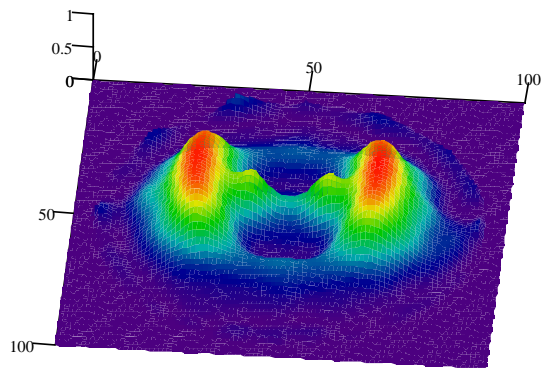
Amplitude

Amplitude



Phase

Phase



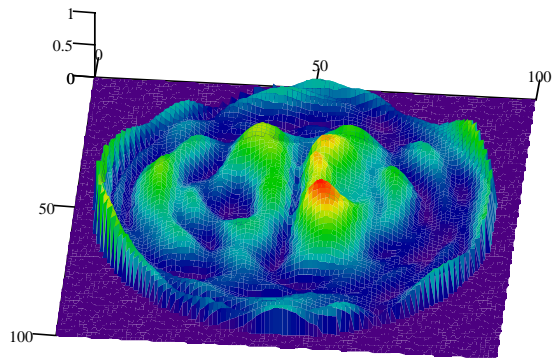
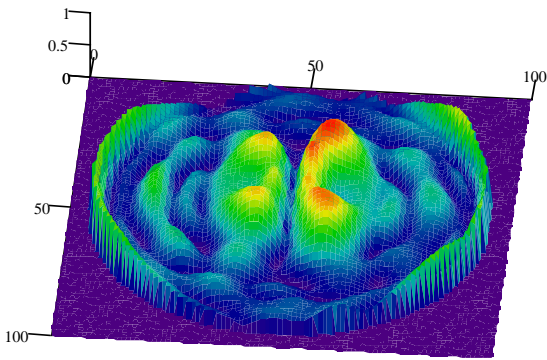
Intensity

Intensity

**Figure 10.** 1/3 Center block. **A)** Theoretically predicted and **B)** Experimentally measured amplitude, phase, and intensity.

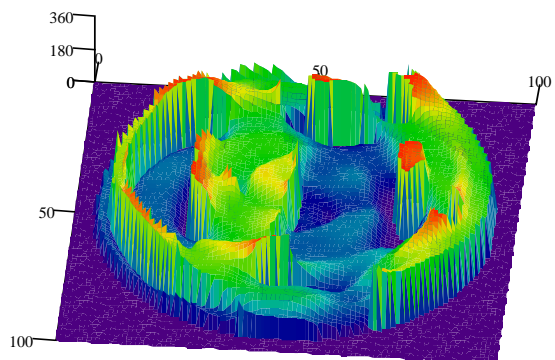
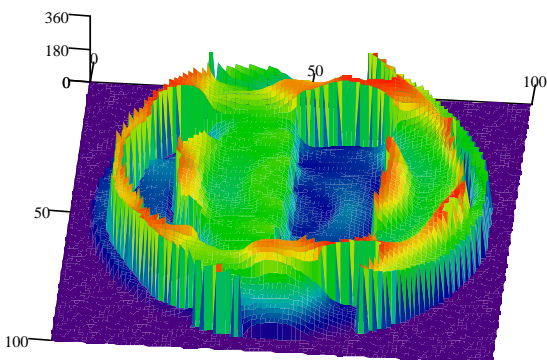
### A) Gaussian Model

### B) Measured



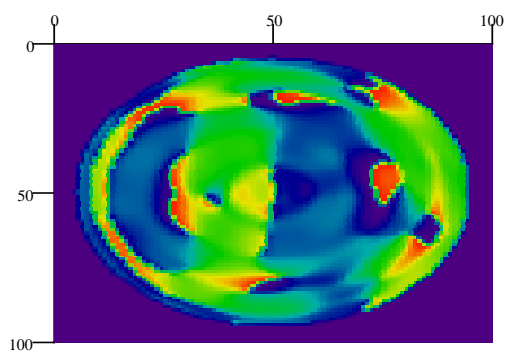
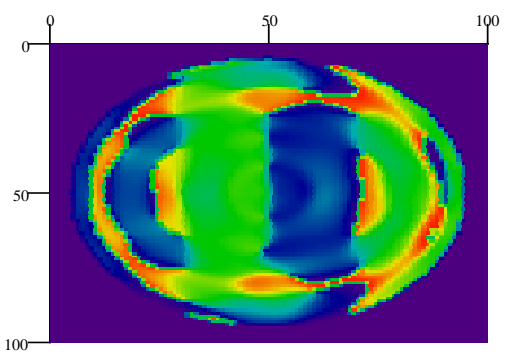
Amplitude

Amplitude



Phase

Phase



Phase

(Top View)

Phase

(Top View)

**Figure 11.** 1/2 Dielectric block - Diagonalized. **A)** Theoretically predicted ( $T = 90\%$ ,  $\Delta\theta = 0.9\pi$ ), and **B)** Experimentally measured amplitude and phase. Within the limitations imposed by the 36 Term Zernike expansion, the formation of the phase shift discontinuity caused by the microscope slide edge is visible down the center of the phase image.

The transform is sensitive to systematic errors including source coherence, pixel distribution and geometry, and SLM phase drift that introduce deviations from the ideal basis functions (a strong endorsement for the use of orthogonal basis sets), and hence difficult to apply in practice. However, the transform was successful in bringing out the phase structure of **Figure 11**. Within the limitations imposed by the 36-term expansion, the formation of the phase shift discontinuity caused by the microscope slide edge is visible down the center of the phase image.

It is important to remember that the primary purpose of the experiment is the demonstration of the underlying principles governing FTH imaging. Images shown in **Figures 9–11** do indeed indicate that the basic mechanisms expected, such as Fourier projection, are present and valid. However, care should be taken when interpreting image content as the actual image essentially is filtered through the relatively low-resolution 36-term expansion window. Sharp amplitude and phase structure in the imaged field tends to excite energy into higher spatial modes that will fall outside of the 36-term window and result in image distortion.

#### 4.0 CONSIDERATIONS & EXAMPLE APPLICATIONS

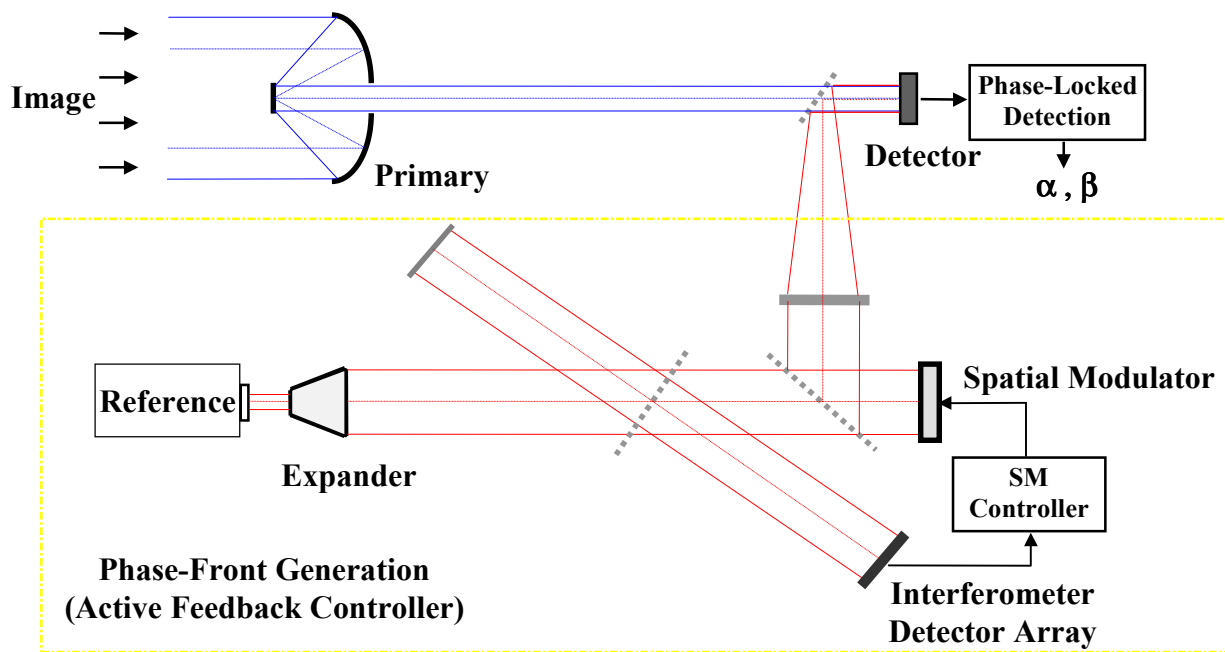


**Figure 12.** Practical FTH receiver. Note that an all-reflective spatial modulator is used in this example.

#### 4.1 Practical Considerations

Practical improvements based on the simple FTH experiment described in **Section 3** are briefly discussed in sections 4.1.A – 4.1.E. Practical considerations include active phase-front correction, phase locked detection, pulsed mode correlated double sample, basis functions, and aperture dimensions based on spatial resolution requirements.

#### 4.1.A. Active Phase-Front Correction

The subsystem generating the spatial phase-fronts will require systematic monitoring and calibration for the removal of phase distortion introduced, for example, by alignment error or modulator drift. Inserting an interferometer into the phase-front beam path is one approach to direct wavefront monitoring of short-wavelength sub-mm through optical systems. Referring to the phase-front generation subsystem of **Figure 12**, as the spatial modulator (SM) scans through pre-programmed phase functions, the interferometer array monitors the phase-front interference distribution and provides corrective feedback through the SM controller. Note that each SM element must be programmable within a spatial phase-shift of at least  $\pm \pi$  (for the wavelength of interest) or larger depending on the feedback algorithm implemented.

#### 4.1.B. Phase Locked Detection (Optical Systems)

FTH systems may be required to acquire Fourier projected coefficients at a high rate of speed. Detection of coefficients requires the precision measurement of the I.F. phase and magnitude. Unlike the simple technique applied in the experiment of **Section 3**, precision high-speed acquisition can be accomplished through techniques employing multi-pulse and I.F. phase-locking<sup>13</sup> for measurement of magnitude and phase ( $\alpha$  and  $\beta$ ).

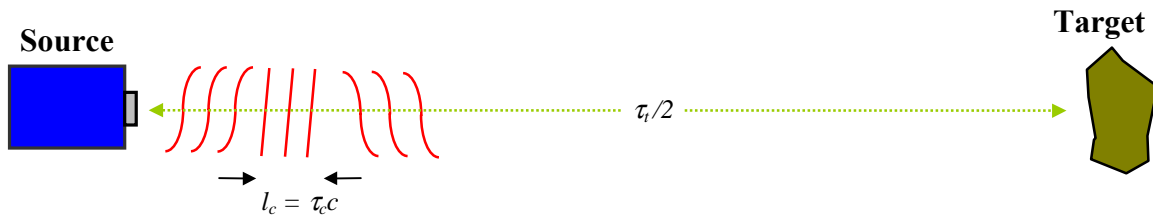


**Figure 13.** Imaging resolution may be limited by the fundamental coherence properties governing Laser and RF sources. Correlated sampling algorithms can aid in mitigating the limitations imposed by a source's finite coherence time,  $\tau_c$ .

#### 4.1.C. Pulsed Mode Correlated Double Sample

FTH imaging resolution can be limited by the fundamental coherence properties governing laser and RF sources. The degradation is a manifestation of transverse amplitude and phase fluctuations on the order of the coherence time<sup>14</sup>,  $\tau_c$ , which is intrinsic to a given coherent source. In essence, source variations cannot be distinguished from image induced modulations, thereby limiting resolution.

What follows is a description of a correlated sampling algorithm that can aid in mitigating the limitations imposed by a source's finite coherence. Correlated double sampling (CDS), as applied to FTH, is the process of removing source fluctuations from the target by correlating the outgoing transmitted pulse to the return, target-modulated pulse, through a common reference.

For example, a pulsed transmitter-receiver system acquiring one coefficient  $C_{m,n}$  per pulse would implement the following algorithm.

- Measure the Fourier projection coefficient,  $C_{X_{m,n}}$ , from the basis function  $\Phi_{m,n}$  of the outgoing transmitted pulse. The measurement must be performed within the sources coherence time  $\tau_c$ .
- Measure the Fourier projection coefficient,  $C_{R_{m,n}}$ , from the basis function  $\Phi_{m,n}$  of the target-modulated return pulse (after a transit time  $\tau_t$ ).
- Subtract the common transverse amplitude and phase error:  

$$C_{m,n}\Phi_{m,n} = (C_{R_{m,n}} - C_{X_{m,n}})\Phi_{m,n} \rightarrow C_{m,n} = C_{R_{m,n}} - C_{X_{m,n}}$$

As both the outgoing and return pulses are compared to a common reference, it is essential that the reference field is properly conditioned (for example, spatially and/or temporally filtered) and stationary over the transit time  $\tau_t$ . Note that as an additional benefit to employing CDS, any stationary spatial phase or amplitude structure in the reference field will be subtracted out.

#### 4.1.D. Basis Functions

FTH receivers, in general, may implement basis functions in which both amplitude and phase are modulated. Complex modulators are practical only if they can achieve sufficiently high modulation rates and are readily calibrated. Systems in which the phase is modulated through a refractive/reflective element or a RF phased array are referred to as pure phase modulators. From **Equation 12**, pure phase modulation requires the phase function argument

$$\theta(x, y) = i \ln \left( \frac{1}{\rho'(x, y)} \Phi_{Ref}(x, y) \right), \quad [23]$$

remain real for synthesis with a refractive or reflective spatial modulator. For example, the familiar two-dimensional Cartesian exponential Fourier series ( $x, y$  normalized to a unit square)

$$\Phi_{m,n}(x, y) = e^{-i2\pi(m x + n y)}, \quad [24]$$

possesses the real phase function

$$\theta(x, y) = 2\pi(m x + n y). \quad [25]$$

Implementation of **Equation 25** suggests a spatial phase modulator generating an  $x, y$  phase pattern across the modulator with slope proportional to  $m, n$  respectively. Furthermore, as coherent fields are longitudinally periodic, the spatial phase “wraps around” every  $2\pi$ , limiting the dynamic modulation requirements to  $\pm \pi$ .

#### 4.1.E. Aperture Diameter

Field imaging, as does any other electromagnetic imaging technology, requires the appropriate matching of the receiver aperture diameter to a given set of resolution requirements. To resolve a target feature size,  $\delta$ , at range  $R$  and wavelength  $\lambda$  will require a minimum aperture diameter of<sup>15</sup>

$$D_o = 2.44 R \frac{\lambda}{\delta} \quad [m]. \quad [26]$$

#### 4.2 Example Applications

Several potential RADAR/LIDAR applications exploiting spatial field imaging are presented in **Figures 14 - 17**. For clarity, the examples focus on the spatial concepts discussed in this paper. However, due to the complimentary nature of the spatial/temporal heterodyne detection process, any practical system design would by necessity focus on the functional integration of FTH concepts within today's highly developed RADAR/LIDAR infrastructure.

Spatial signature discrimination and Doppler field imaging concepts allowing enhanced target classification and/or identification are illustrated in **Figures 14** and **15** respectively, while **Figure 16** provides an example of electronic counter measure (ECM) suppression through spatial field filtering. The ECM suppression principles of **Figure 16** are similar to techniques already practiced in current RF RADAR systems deploying phased array receivers.<sup>16,17</sup> From **Equation 26**, aperture diameters at longer RF wavelengths ( $> \text{cm}$ ), can become prohibitively large for high resolution at long ranges. Referring to **Figure 17**, resolution and sensitivity may be enhanced with a sparse array of coherently phased receivers. The total induced signal, given the scattered image field ( $\Phi_{Image}$ ) and the 3-D surface formed by the receiver aperture and reference field ( $\Phi_{Ref}$ ) discretely sampled at  $\mathbf{r}_i$ , is defined through the spatial projection operator (**Equation 16**)

$$\iint_s \mathbf{J} \cdot d\mathbf{s} = k \iint_s \eta(\mathbf{E} \times \mathbf{H}) \cdot d\mathbf{s} \Rightarrow \sum_i C_i = \sum_i \langle \Phi_{Ref}(\mathbf{r}_i, t, \mathbf{p}, \lambda), \Phi_{Image}(\mathbf{r}_i, t, \mathbf{p}, \lambda) \rangle. \quad [27]$$

**Equation 28** relates the coherent summation of the projection coefficients,  $C_i$ , to the spatial projections of the image and reference field surfaces evaluated over the receiver aperture at location  $\mathbf{r}_i$ . Receivers phasing ( $\Phi_{Ref}$ ) is accomplished through addition or subtraction of phase pedestal offsets at the receiver local oscillator and delay offsets to the  $C_i$  before summation.

As a practical note, the target reflected phase fronts of examples **Figure 14 - 17** may exceed a wavelength in depth, leading to  $\pm \pi$  phase ambiguities in the retrieved images. For applications requiring preservation of phase depth, the ambiguities may be resolved through multiple wavelength interferometry<sup>18</sup> where the target is illuminated and imaged, preferably simultaneously, with two or more wavelengths resulting in the two-dimensional synthetic phase image:

$$\phi_{\lambda_s}(x, y) = \phi_{\lambda_1}(x, y) - \phi_{\lambda_2}(x, y), \quad \text{where } \lambda_s = \frac{\lambda_1 \lambda_2}{|\lambda_1 - \lambda_2|}. \quad [28]$$

The technique may also be used to reduce image phase sensitivity due to fluctuations resulting from moving target dynamics (target scintillation).

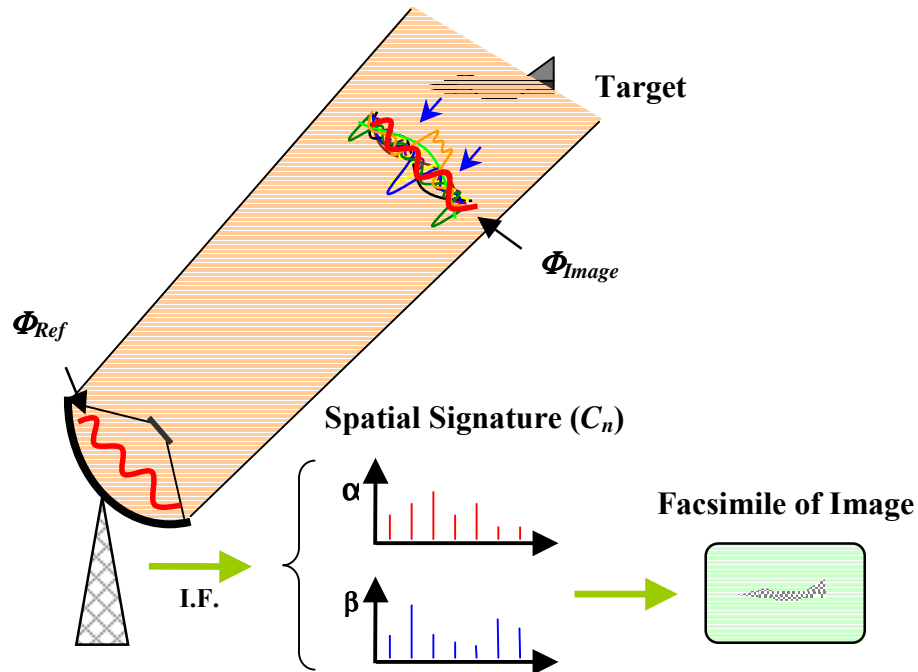


**Figure 14.** Field imaging – spatial signature discrimination. Field imaging may be a useful tool to aid or enhance RADAR/LIDAR target classification and identification. Real-time configurable spatial reference functions permit the synthesis of adaptive spatial filters and/or optimal detection algorithms.

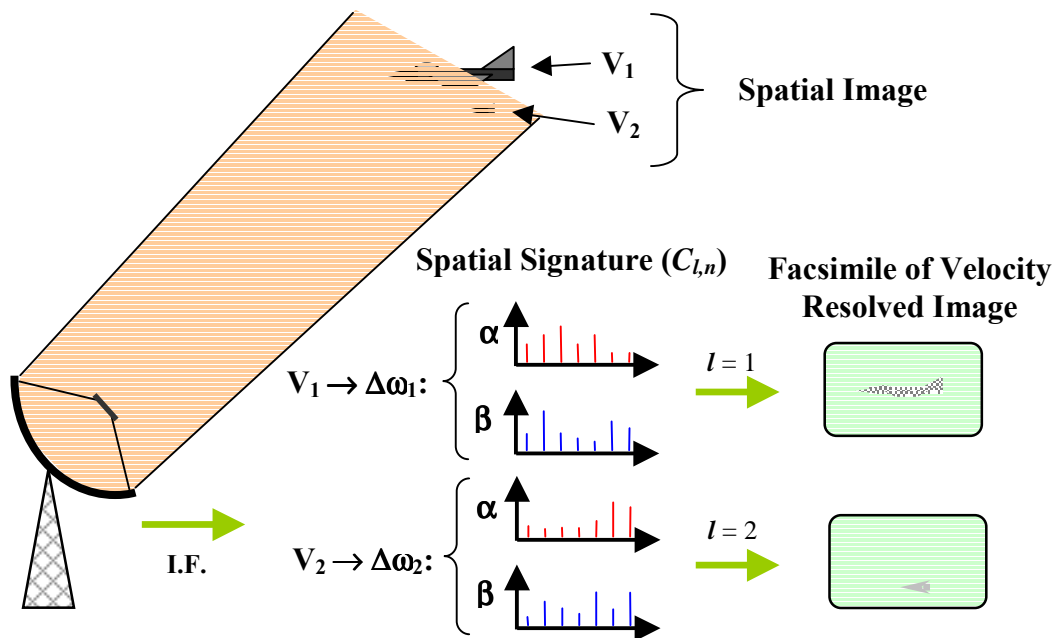


**Figure 15.** Doppler imaging – velocity field discrimination. Spatially distinguishable targets may be velocity resolved through the (temporal) frequency filtering of Doppler shifted spatial Fourier coefficients,  $C_{l,n}$ .  $l$  is the Doppler shifted index representing the  $l^{th}$  I.F. bandpass frequency,  $\Delta\omega$ , (see Equations 13-14).

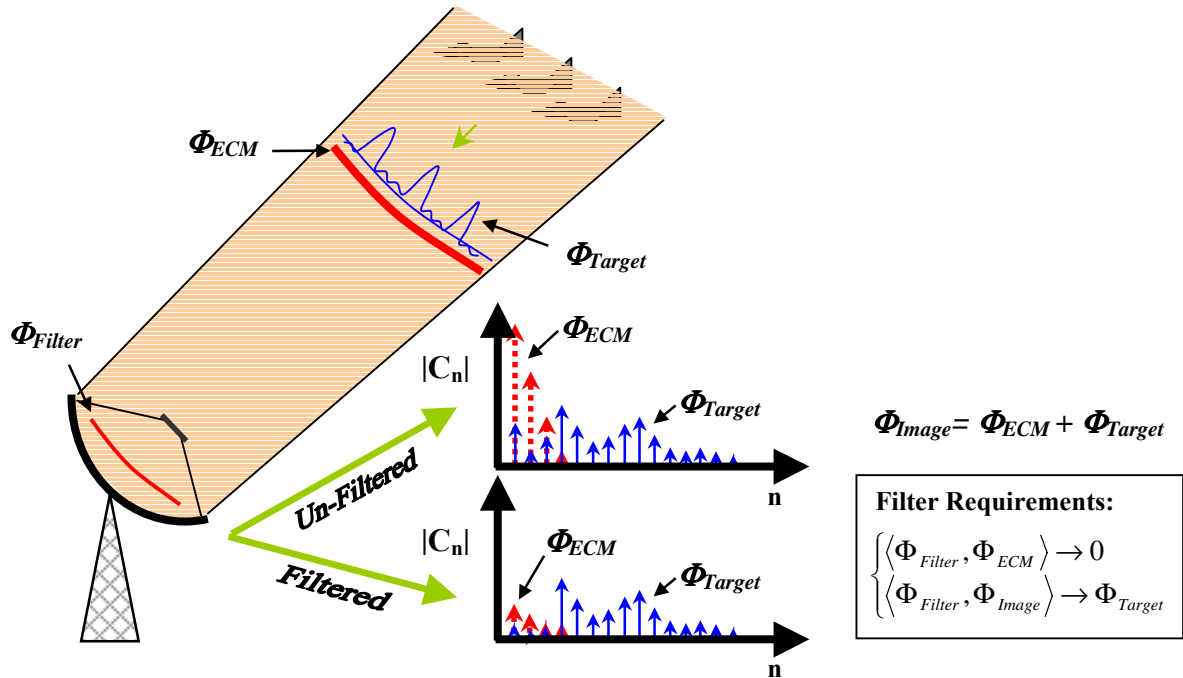


**Figure 16.** Spatial field filtering - electronic counter measures suppression. Provided the target signature is spatially distinguishable from the Electronic Counter Measure (ECM) signature, field based spatial filtering can potentially aid in discriminating the desired target(s),  $\Phi_{Target}$ , from the unwanted ECM induced clutter and noise,  $\Phi_{ECM}$ . Shown in the above example, spatial filtering is accomplished by first pre-sampling the image field,  $\Phi_{Image}$ , followed by the construction of a reference set with components orthogonal to the ECM spatial signature. The spatial filter coherently nulls (through orthogonal field projection) the lower-order spatial ECM components at the detector (before entering the I.F. circuitry), while passing the higher order target signature.

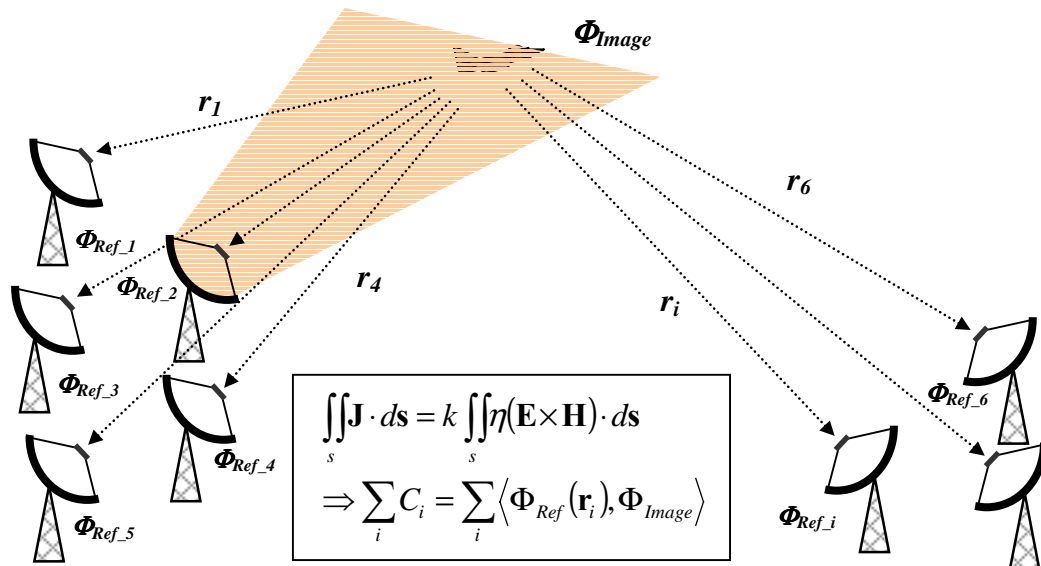


**Figure 17.** Coherently phased sparse-array. Coherently phased sparse arrays for improved spatial resolution and detection of low cross-section targets. Receivers phasing ( $\Phi_{Ref}$ ) is accomplished through addition or subtraction of phase pedestal offsets at the receiver local oscillator and delay offsets to the  $C_i$  before summation.

## 5.0 Conclusion

We have demonstrated a detection process capable of directly imaging the transverse amplitude, phase, and Doppler shift of coherent electromagnetic fields. The detection process, Fourier Transform Heterodyne, incorporates Fourier projection principles through transverse spatial encoding of the local oscillator for field imaging. Appropriate selection of spatial encoding functions allows image retrieval by way of classic Fourier manipulations. The underlying principles governing FTH imaging were demonstrated via a simple experimental setup based on a HeNe laser and a 69 element spatial phase modulator. Several potential RADAR/LIDAR applications exploiting spatial field imaging were presented.

## REFERENCES

- 
- <sup>1</sup> M. Born and E. Wolf, *Principles of Optics*, Cambridge University Press, 6<sup>th</sup> Ed., 1980.
  - <sup>2</sup> J. W. Goodman, *Introduction to Fourier Optics*, McGraw-Hill, 1968.
  - <sup>3</sup> G. O. Reynolds, J. B. DeViles, G. B. Parrent and Brian J. Thompson, *Physical Optics Notebook Tutorials In Fourier Optics*, SPIE and American Institute of Physics, pp. 94-96, 1989.
  - <sup>4</sup> C. A. Balanis, *Antenna Theory Analysis and Design*, pp. 797-801, John Wiley & Sons, 2<sup>nd</sup> Ed., 1997.
  - <sup>5</sup> J. D. Jackson, *Classical Electrodynamics*, John Wiley & Sons, 2<sup>nd</sup> Ed., 1975.
  - <sup>6</sup> S. C. Cohen, "Heterodyne Detection: Phase Front Alignment, Beam Spot Size, and Detector Uniformity," *Applied Optics*, Vol. 14, No. 8, pp. 9153-1958, Aug. 1975.
  - <sup>7</sup> S. Fowler, G. W. Kamerman, and G. Lawson, "Analysis of Heterodyne Efficiency for Coherent Laser Radars," *SPIE Applied Laser Radar Technology*, Vol. 1936, pp. 137-146, 1993.
  - <sup>8</sup> F. B. Hildebrand, *Advanced Calculus for Applications*, pp. 203-209, Prentice-Hall, 2<sup>nd</sup> Ed., 1976.
  - <sup>9</sup> C. A. Balanis, *Antenna Theory Analysis and Design*, pp. 309-324, John Wiley & Sons, 2<sup>nd</sup> Ed., 1997.
  - <sup>10</sup> J. Y. Wang and D. E. Silva, "Wave-Front Interpretation With Zernike Polynomials," *Applied Optics*, Vol. 19, No. 9, pp. 1510-1513, May 1980.
  - <sup>11</sup> K. Chang, *Handbook of Microwave and Optical Components Vol. 3*, pp. 28-32, John Wiley & Sons, 1990.

---

<sup>12</sup> O. K. Ersoy, *Fourier-Related Transforms, Fast Algorithms and Applications*, Prentice Hall, 1997.

<sup>13</sup> F. M. Gardner, *Phaselock Techniques*, John Wiley & Sons, 1979.

<sup>14</sup> J. W. Goodman, *Statistical Optics*, John Wiley & Sons, 1985.

<sup>15</sup> B. J. Cooke, B. E. Laubscher, M. Cafferty, N. L. Olivas, M. J. Schmitt, K. R. Fuller, R. M. Goeller, D. E. Mietz, J. J. Tiee, R. K. Sander, J. L. Vampola, S. L. Price, and I. Kasai, "Analysis and Design Methodology for the Development of Optimized, Direct-Detection CO<sub>2</sub> DIAL Receivers," *SPIE Infrared Instrumentation VII*, 1997.

<sup>16</sup> M. I. Skolnik, *Introduction to Radar Systems*, pp. 547-553, McGraw-Hill, 1980.

<sup>17</sup> K. Chang, *Handbook of Microwave and Optical Components Vol. 1*, pp. 675-702, John Wiley & Sons, 1989.

<sup>18</sup> L. McMackin, D. G. Voetz, and M. P. Fetrow, "Multiple Wavelength Heterodyne Array Interferometry," *Opt. Express* *l.*, 1997.